




Cleavage fracture micromechanisms in thick-section quenched and tempered S690 high-strength steels

Virgínia Bertolo^{1,*} , Quanxin Jiang¹, Urša Tiringier¹, Carey L. Walters^{2,3}, Jilt Sietsma¹, and Vera Popovich¹

¹Department of Materials Science and Engineering, Delft University of Technology, Mekelweg 2, 2628 CD Delft, The Netherlands

²Structural Dynamics, TNO, Leeghwaterstraat 44, 2628 CA Delft, The Netherlands

³Maritime and Transport Technology, Delft University of Technology, Mekelweg 2, 2628 CD Delft, The Netherlands

Received: 7 June 2022

Accepted: 9 October 2022

© The Author(s) 2022

ABSTRACT

For structural assessment and optimal design of thick-section high-strength steels in applications under harsh service conditions, it is essential to understand the cleavage fracture micromechanisms. In this study, we assess the effects of through-thickness microstructure of an 80-mm-thick quenched and tempered S690 high-strength steel, notch orientation, and crack tip constraint in cleavage nucleation and propagation via sub-sized crack tip opening displacement (CTOD) testing at $-100\text{ }^{\circ}\text{C}$. The notch was placed parallel and perpendicular to the rolling direction, and the crack tip constraint was analysed by varying the a/W ratio: 0.5, 0.25, and 0.1. The notch orientation does not play a role, and the material is considered isotropic in-plane. Nb-rich inclusions were observed to act as the weak microstructural link in the steel, triggering fracture in specimens with the lowest CTOD values. While shallow-cracked specimens from the top section present larger critical CTOD values than deep-cracked ones due to stress relief ahead of the crack tip, the constraint does not have a significant influence in the middle due to the very detrimental microstructure in the presence of Nb-rich inclusions. Some specimens show areas of intergranular fracture due to the combined effect of C, Cr, Mn, Ni, and P segregation along with precipitation of Nb-rich inclusions clusters on the grain boundaries. Several crack deflections at high-angle grain boundaries were observed where the neighbouring sub-structure has different Bain axes.

Handling Editor: Megumi Kawasaki.

Address correspondence to E-mail: v.moretebarbosabertolo@tudelft.nl

<https://doi.org/10.1007/s10853-022-07841-1>

Published online: 15 October 2022

Introduction

Cleavage fracture, as the most dangerous form of fracture, raises concern in structural components under harsh operating conditions. Although high-performance materials with an optimal combination of strength and toughness, such as high-strength steels (HSSs), are often selected for structural applications, severe operating conditions can make them susceptible to brittle fracture [1–3]. For example, thick-section HSSs are applied in offshore structures, including equipment necessary for installing green energy farms and decommissioning old structures that had been used for the exploitation of oil and gas. In such applications, the service environments account for the presence of high stresses and the potential of very low temperatures. As body-centred cubic (BCC) HSSs are known to transition from ductile to brittle when the temperature is reduced or high strain rates are applied, the potential for catastrophic cleavage fracture exists. Cleavage is the governing micromechanism in the ductile-to-brittle transition region and the lower shelf [4]. Hence, for integrity assessment and optimal material design of these structures, including modelling approaches, the investigation of cleavage initiation and propagation micromechanisms of thick-section HSSs is required. The influence of microstructural factors on cleavage fracture toughness and micromechanisms has been investigated in the literature [5–10]. However, there are still some knowledge gaps to be filled.

First, from the microstructural point of view, thick-section HSSs display complex and multiphase microstructures with a significant degree of inhomogeneity through the thickness (e.g. grain size, inclusions, and phase fractions) [5, 11, 12]. Consequently, a considerable scatter of mechanical and fracture properties is observed along the thickness [5, 6, 12, 13], resulting in great consequences for accurate structural integrity evaluation and definition of structural design specifications. To assess cleavage fracture for such steel plates, many experimental studies found in the literature use Charpy testing, which has limitations regarding specimen plastic constraint—blunt notch instead of a sharp crack—strain rate—dynamic loading instead of quasi-static loading—and specimen size and size-dependent property—relatively small, not representing metallurgical structural variations and material true property [5, 12, 13]. Another limitation of these studies is that they are

mostly focused on modified or experimental steels that are not used in industrial practice. Thus, they do not necessarily have the actual heterogeneous microstructures observed in operating structural components [12, 13]. Moreover, they lack sufficiently detailed material characterisation to allow for an accurate and comprehensive analysis of cleavage fracture [5, 6, 12, 14]. Hence, these studies do not provide a representative understanding of the involved fracture micromechanisms, crack initiation and propagation, in structures. For instance, Pallaspuro et al. [13] carried out a similar study where a comprehensive and statistical microstructural characterisation is provided. However, the steel is experimental, where material from different positions is separately hot-rolled and heat-treated, resulting in a different microstructure and mechanical and fracture properties representative of real commercial steels. Liu, Zhang and Li, and Wang et al. [5, 12] also investigated the scatter of properties through the thickness of thick-section steels connecting it with microstructural features. These studies were carried out in steels that are not commercial but are subjected to similar industrial processing routes. However, the authors do not provide sufficient statistical microstructural information for the assessment of various microstructures features on the onset and propagation of cleavage cracks. Moreover, fracture is evaluated in terms of impact toughness via Charpy tests.

Studies related to micromechanism-driven modelling of cleavage fracture share this knowledge gap. In a multi-barrier theory, cleavage fracture of ferritic steels is regarded as the result of the successive occurrence of three microscale events: nucleation of a slip-induced crack at a brittle second-phase particle (i.e. carbides in steels) or inclusion; propagation of the microcrack across the particle/matrix interface under the local stress state; and propagation of the grain-sized crack to neighbouring grains across the grain boundary under the local stress state [15–18]. Hence, the use of a multi-barrier theory requires an understanding of the relationship between representative and statistical microstructure, local properties, and failure micromechanisms. Bimodal methods in cleavage simulations of steels have modelled macroscopic microstructural inhomogeneities at the millimetre scale [19, 20]. However, microstructural inhomogeneities below the millimetre scale have not yet been considered.

Second, from the experimental perspective, fracture toughness testing and assessment are standardised, e.g. [21, 22]. However, there are some variables in the fracture toughness testing that may have a significant effect on the resulting toughness values. For instance, research has shown that the orientation of the notch may affect the toughness, reflecting an anisotropic behaviour of the material and indicating the most critical crack orientation in the structure [7, 23]. The crack tip constraint and its effect on fracture toughness are also extensively studied in the literature [8, 9, 24–26]. The crack tip constraint is related to the stresses at the crack tip. In standard fracture assessments, deep-cracked specimens ($0.45 \leq a/W \leq 0.55$, where a is the nominal crack length and W is the specimen width) are used to restrict the plastic zone near the crack tip, resulting in very small plastic zones compared to the specimen dimensions. Hence, a high degree of stress triaxiality (constraint) in the crack tip is ensured. This procedure follows a conservative approach and measures a lower-bound value for the material's fracture toughness. However, structural components may contain initial surface (shallow) cracks originating from welding and corrosion processes. In this case, when the material is loaded, the plastic deformation at the crack tip may expand to the nearest free surface, relaxing the stresses at the crack tip and reducing the constraint. Consequently, shallow-cracked specimens are likely to have higher fracture toughness than deep-cracked specimens [9, 10, 26, 27]. Sorem, Dodds, and Rolfe [10] reported that shallow-cracked specimens ($a/W = 0.15$) of a low-strength structural steel have critical CTOD values: 2.5 times higher than deep-cracked specimens ($a/W = 0.5$) within the lower transition region. Also, the crack tip constraint was observed to affect the toughness-temperature relationship, which is important for BCC steels [26, 27]. As stresses ahead of the crack tip are relieved with the loss of constraint in the shallow-cracked specimens, larger far-field stresses need to be reached for brittle fracture to occur and cleavage is delayed in relation to the deep-cracked specimens. A difference of 20 °C in the transition temperature between deep- and shallow-notched specimens for a low-strength structural steel was observed by Sorem, Dodds, and Rolfe [26]. Thus, standard procedures may be considered too conservative for actual structures with shallow cracks, and the material fracture behaviour with shallow defects is worth investigating for a

realistic practical fracture integrity assessment. As discussed, extensive research has been done to address the impact of crack depth and plastic constraint on fracture toughness. Nevertheless, the influence of the material microstructure on the plastic constraint effect in HSSs still needs to be investigated.

Therefore, the effects of through-thickness microstructural inhomogeneity on cleavage fracture toughness are comprehensively investigated to identify the microstructural features governing cleavage fracture in HSSs. Bertolo et al. [11] extensively and statistically characterised the through-thickness microstructure of the steel studied herein. In the present work, the cleavage fracture toughness of the investigated high-strength steel is assessed via three-point bend crack tip opening displacement (CTOD) tests on a commercially available 80 mm thick S690QL HSS plate at -100 °C, to evaluate the material on the lower shelf. Three macroscopic variables were considered in the CTOD tests for further examination: (1) crack orientation with respect to the rolling direction to analyse whether the material presents anisotropic behaviour, (2) crack depth to understand the constraint effects on toughness in the present material/microstructure under study, and (3) through-thickness position to understand through-thickness homogeneity. Afterwards, fracture surfaces and their transversal planes were analysed, providing an extensive statistical analysis of cleavage initiation sites, showing the direct effect of different initiation sites on fracture toughness and the preferential propagation paths. The outcome of this research along with the work carried out in [11] represents a unique data set that relates the micro- and macro-scales relevant for understanding cleavage fracture in HSSs and modelling it using the multi-barrier theory.

Material and methods

Material

The investigated materials were taken from the top quarter (further referred to as top) and middle thickness sections of a commercially available 80-mm-thick quenched and tempered (S690QL according to EN 10025-6 [28]) high-strength steel plate. The chemical composition of these sections, measured by X-ray fluorescence (XRF) and LECO

Table 1 Chemical composition of S690QL at two through-thickness locations

| wt (%) | Fe | C | Si | Al | Mo | Other |
|--------|-----|---------------|---------------|---------------|---------------|----------------------------|
| Top | Bal | 0.170 ± 0.001 | 0.290 ± 0.022 | 0.070 ± 0.005 | 0.300 ± 0.007 | Mn, Ni, Cr, Nb, P, N, S, B |
| Middle | Bal | 0.160 ± 0.001 | 0.30 ± 0.03 | 0.080 ± 0.011 | 0.29 ± 0.02 | |

combustion analysis, is given in Table 1. The elemental content of this steel is in accordance with the standard EN 10025-6, including for the ones under “other” (max wt% of Mn = 1.7, Ni = 4.0, Cr = 1.5, Nb = 0.06, P = 0.02, N = 0.015, S = 0.01 and B = 0.005) [28]. The tensile and micro-Vickers hardness properties for the top and middle sections at room temperature and $-100\text{ }^{\circ}\text{C}$ are presented in Table 2. The material was measured to have an isotropic in-plane behaviour.

An in-depth microstructural characterisation of both thickness positions was performed and is discussed in detail in [11]. Figure 1 exemplifies the microstructure and inclusions found in the through-thickness of the S690QL high-strength steel. Table 3 summarises the main microstructural characteristics. The through-thickness microstructural matrix of the HSS plate under study is a mixture of tempered (between 600 and 650 $^{\circ}\text{C}$ for a few minutes) microconstituents ferrite (F), bainite (TB), and martensite (TM). Additionally, centreline segregation bands (SB) were observed in the mid-thickness section, with different phase fractions of the middle section outside SB. Based on the grain average image quality (GAIQ) analysis, the phase fraction of F, TB, and TM is: 6%, 68%, and 22% (top); 15%, 76%, and 7% (middle section outside SB); and 0.2%, 86% and 14% (middle section inside SB). Prior austenite grains (PAG) are larger in the middle section than in the top section, except for the segregation bands where PAG are smaller within the middle and comparable to the grains in the top section. In general, the top and middle sections display spherical and cubic inclusions with complex chemical compositions with a

mixture of oxides, carbides, and nitrides (e.g. (Mg, Ca, Al, Ti)(O, N) and (Nb, Ti)(N, C)). Nb-rich cubic inclusions are often observed distributed as clusters and associated with defects (e.g. cracks in the inclusions themselves and voids in the interface inclusion/matrix). These inclusions were quantified, and their sizes were measured. It was observed that bigger-spherical and cubic-inclusions are presented in a larger area fraction in the central part of the steel plate than on the outer surface [11]. A distinct hardness gradient is observed through the plate's thickness. The top section shows higher hardness than the middle section. However, a hardness maximum, comparable to the value in the top section, right in the centre of the plate is observed. This is related to the area fraction of martensite and PAG sizes. The top section, as well as the segregation bands, has a larger area fraction of martensite and smaller PAG sizes than the middle section outside the segregation bands, resulting in higher hardness. Moreover, the segregation bands also present clusters of brittle inclusions which explains their nanohardness being up to 2.4 times higher than in the surrounding areas in the middle section.

Methods

Characterisation of fracture properties

Three-point bending tests using sub-sized single edge-notched bending (SENB) specimens from the top and middle sections were carried out similar to the ISO 12135 standard [21] at $-100\text{ }^{\circ}\text{C}$ and a deformation rate of 2 mm/s using a 350 kN MTS 858

Table 2 Tensile and Micro-Vickers hardness properties of the top and middle sections at $-100\text{ }^{\circ}\text{C}$ and room temperature (RT)

| Thickness position | Yield strength (MPa) | | Tensile strength (MPa) | | Micro-vickers hardness (HV3) |
|--------------------|----------------------|--------------------------------|------------------------|--------------------------------|------------------------------|
| | RT | $-100\text{ }^{\circ}\text{C}$ | RT | $-100\text{ }^{\circ}\text{C}$ | RT |
| Top | 811 ± 4 | 974 ± 13 | 931 ± 4 | 1078 ± 14 | 280 ± 5 |
| Middle | 739 ± 11 | 895 ± 12 | 861 ± 12 | 1013 ± 13 | 272 ± 11 |

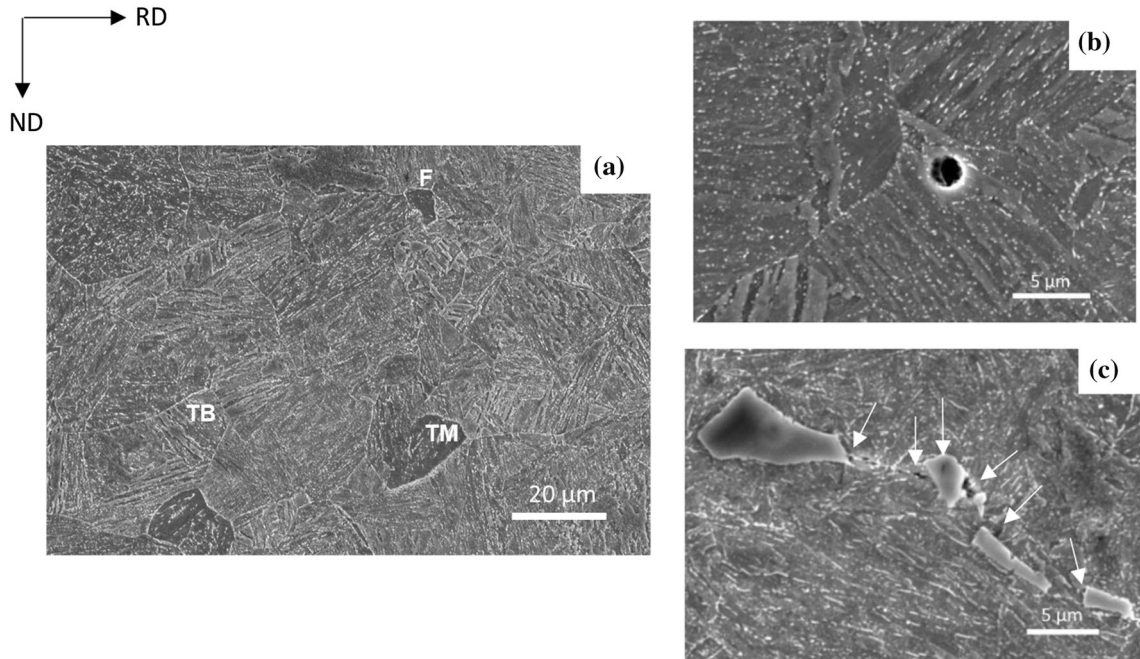


Figure 1 SEM micrographs of the (a) tempered microconstituents, ferrite, bainite, and martensite, and b (Mg, Al, Ca)(O, S) and c (Nb, Ti)(C) inclusions that constitute the

through-thickness microstructure of the S690QL steel. Defects associated with inclusions and the interface inclusion/matrix are indicated by the white arrows (Partially included in [29]).

Table 3 Summary of microstructural quantitative characteristics for the S690QL high-strength steel under study reported in [11]

| Thickness position | Average PAG size (Intercept) (μm) | | Inclusions | | | | |
|--------------------|-----------------------------------|------------|----------------|------------|---|--------------|--------------------------------------|
| | | | Shape | Range (μm) | Area fraction | Fraction (%) | Fraction of clustered inclusions (%) |
| Top | 19.2 ± 1.4 | | Oxide-circular | 1–5 | $5 \times 10^{-4} \pm 3 \times 10^{-4}$ | 88 ± 1 | – |
| Middle | Outside SB | 23.5 ± 2.3 | Nb-cubic | 1–7 | $7 \times 10^{-5} \pm 4 \times 10^{-5}$ | 12 ± 1 | 47 |
| | | | Oxide-circular | 1–5 | $7 \times 10^{-4} \pm 3 \times 10^{-4}$ | 76 ± 6 | – |
| | Inside SB | 19.1 ± 2.6 | Nb-cubic | 1–12 | $2 \times 10^{-4} \pm 3 \times 10^{-5}$ | 24 ± 6 | 74 |

SB segregation bands

servo-hydraulic test rig. First of all, a thermocouple is spot welded to the specimen to monitor the temperature during cooling and testing. Next, the specimen is cooled down by immersion in liquid nitrogen until, approximately $-196\text{ }^{\circ}\text{C}$ (liquid nitrogen's boiling temperature). The temperature difference between the minimum cooling temperature and the test temperature is to allow for thermal soaking and to ensure there is enough time to mount the specimen in the set-up. Subsequently, the specimen is placed on the machine, touching a thermal insulation material placed next to the rollers (at a larger height) of the

three-point bending set-up. The aim is to avoid the specimen to touch the metallic rollers before that test and avoid the fast heat exchange. Finally, a pre-load is applied to make contact between rollers-specimen and when the specimen reaches $-100\text{ }^{\circ}\text{C}$, the test is performed. This test temperature ($-100\text{ }^{\circ}\text{C}$) is much lower than the temperatures experienced in offshore and maritime applications as the aim is to perform tests in the cleavage fracture regime. Although the studied S690QL steel fully satisfies the design requirements for offshore and maritime applications,

it may exhibit weaknesses under these more severe test conditions which impact its performance.

Different experimental conditions were taken into account regarding crack orientation, T–L (parallel to the rolling direction) and L–T (perpendicular to the rolling direction), and crack depth (a/W), 0.5, 0.25 and 0.1 to vary the crack tip constraint from high to low conditions (Fig. 2). Specimens with $a/W = 0.5$ will be referred to as high-constraint; $a/W = 0.25$ will be referred to as mid-constraint; $a/W = 0.1$ will be referred to as low-constraint. Details on the specimen's dimensions and conditions are given in Fig. 2. The dashed grey semi-circles represent the three-point bending rollers.

The CTOD results for shallow notches, $a/W = 0.1$ and 0.25, were calculated according to the ISO 12135 standard [21]. CTOD fracture toughness tests are based on the plastic hinge model. For the shallow-cracked specimens, the plastic hinge point location in the unnotched ligament ahead of the crack tip can be shifted due to the smaller a/W ratio than in the conventional deep-cracked specimens. Some studies reported a significantly lower value of the rotational factor (r_p) for the shallow-cracked specimens compared to the 0.4 used in the standards for deep-cracked specimens [21]. For instance, it was estimated at 0.2 for $a/W = 0.1$ [30, 31]. Hence, it is essential to determine the r_p values for shallow-cracked specimens for an accurate fracture toughness measurement of structures having surface defects. The values of r_p for a/W of 0.1 and 0.25 were determined through finite element analyses by [32]. The shallow-cracked specimens were modelled in three dimensions with

appropriate boundary conditions reproducing the experimental set-up. For a/W of 0.1, the total initial crack length used was 2 mm, which includes a 0.6-mm-long notch and a 1.4-mm-long pre-fatigued crack. For a/W of 0.25, the total initial crack length used was 5 mm, which includes a 3.5-mm-long notch and a 1.5-mm-long pre-fatigued crack. The crack tip was modelled with an initial blunted opening with a radius of 0.005 mm. The finite element models were loaded by a displacement ramp imposed on the loading point through a rigid roller. The plastic rotational factor, r_p , is calculated from its relationship with CTOD and crack mouth opening displacement (CMOD):

$$\delta_p = \frac{r_p(W-a)V_p}{r_p(W-a)+a} \quad (1)$$

where δ_p is the plastic CTOD component and V_p is the plastic CMOD measured from the finite element model. As results of the finite element analyses, r_p values were calculated as 0.24 and 0.31 for a/W of 0.1 and 0.25, respectively. The failure probability of a specimen was calculated as a rank probability:

$$\text{Failure probability} = \frac{(i-0.3)}{(N+0.4)} \quad (2)$$

where i is the rank number in terms of CTOD and N is the total number of experiments.

Characterisation of fracture surface and profile

SENB fractured surfaces were investigated to study the fracture micromechanisms (e.g. crack initiation

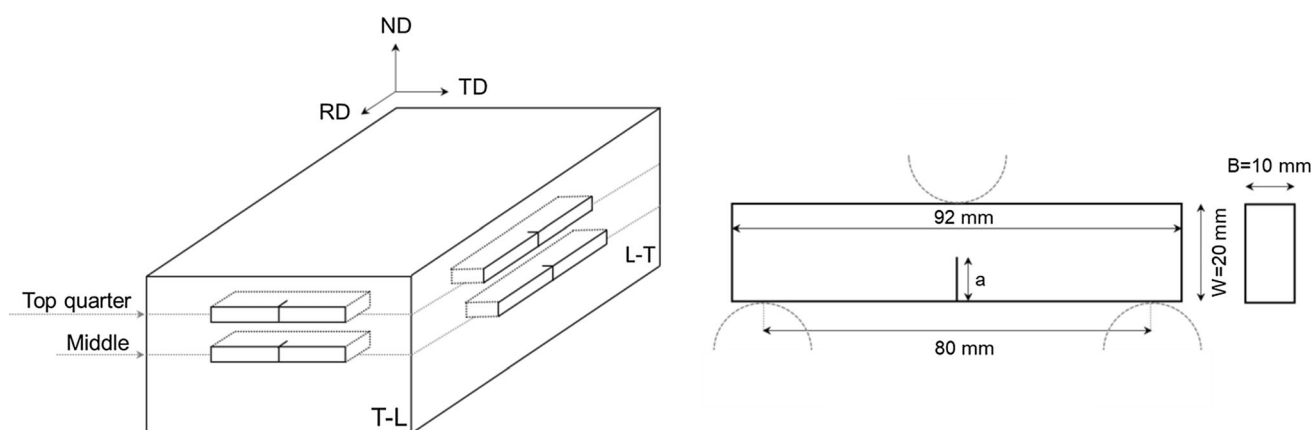


Figure 2 Schematic illustration showing how SENB specimens were extracted from the steel plate in terms of thickness position and notch orientation to the RD, and SENB specimen's

dimensions. The dashed grey semicircles represent the three-point bending rollers. ND is the normal direction, RD is and rolling direction, and TD is the transverse direction (Adapted from [11]).

and propagation). First, the direct examination of fracture surfaces via scanning electron microscopy (SEM) equipped with electron dispersive spectroscopy (EDS) provided information on the mode of failure and identification of initiation sites. Second, to identify the cleavage micromechanisms involved in the crack propagation process of the S690QT high-strength steel, the transverse section of the fractured surface of SENB specimens (hatched area in Fig. 3b) tested at $-100\text{ }^{\circ}\text{C}$ was analysed by SEM and electron backscattered diffraction (EBSD). Specimens from the top and middle sections with the notch oriented parallel to the rolling direction (T-L) and with the lowest CTOD values (0.02 mm and 0.01 mm, respectively) were selected for this investigation to study the worst-case scenario. The preparation of the transverse section of the fractured surfaces was done according to the following steps:

1. The distance from the external surface (edge) of the CTOD specimen and the initiation site was measured;
2. The CTOD specimen was mounted in conductive resin to ensure a final flat and well-polished sample where the external cross-section surface of the specimen was the one exposed for metallographic preparation and subsequent analysis;
3. The mounted sample was ground using P80 SiC grinding paper to reduce the sample thickness at a distance mentioned in step 1 (Fig. 3a). Thus, the fracture profile to be analysed would be close to the initiation site and, consequently, represent an area tested under a triaxial stress state (hatched area in Fig. 3b). The surface was further ground with SiC sanding papers of P180, P320, P800, and P1200. Subsequently, samples were polished with $3\text{ }\mu\text{m}$ and $1\text{ }\mu\text{m}$ diamond solution for 25 min per step followed by OPS polishing with $0.25\text{ }\mu\text{m}$ for

1 h. The appearance of the cross-section of the fracture surface is shown in Fig. 3c.

4. The sample was then removed from the resin to avoid drift during the EBSD scans. The analysed areas in the transversal section of the fractured surfaces were located close to the pre-crack tip, where initiation sites were usually located, and where the crack has propagated without considerably changing its path and has also deflected significantly. Then, it is possible to identify microstructural characteristics that have a weak and strong influence on the crack propagation under triaxial stress state.

EBSD data were acquired on a *Thermo-Fisher HeliosTM UXe G4 PFIB* scanning electron microscope equipped with a Field Emission Gun (FEG-SEM) using 20 kV accelerating voltage, 3.2 nA current, tilt angle $70\text{ }^{\circ}\text{C}$, and step size $0.1\text{ }\mu\text{m}$ using TeamTM software and post-processed with EDAX-TSL-OIM AnalysisTM software. The initial post-processing step was the data clean-up. First, grain fit standardisation with a grain tolerance angle of 5° and a minimum grain size of 4 pixels was applied considering that grains contain multiple pixel rows. Secondly, the neighbour orientation correlation procedure with a grain tolerance angle of 5° and a minimum confidence index of 0.1 was used. Lastly, neighbour phase correlation with a minimum confidence index of 0.1 was applied. Afterwards, the final grain definition was done with a tolerance angle of 5° and a minimum size of 4 pixels.

In order to further investigate the regions of the middle section that fractured in an intergranular manner and inspect whether the alloying segregation at the grain boundary is playing a role, a preliminary chemical composition line scan analysis was carried out via Scanning Auger Microprobe (SAM). A PHI-

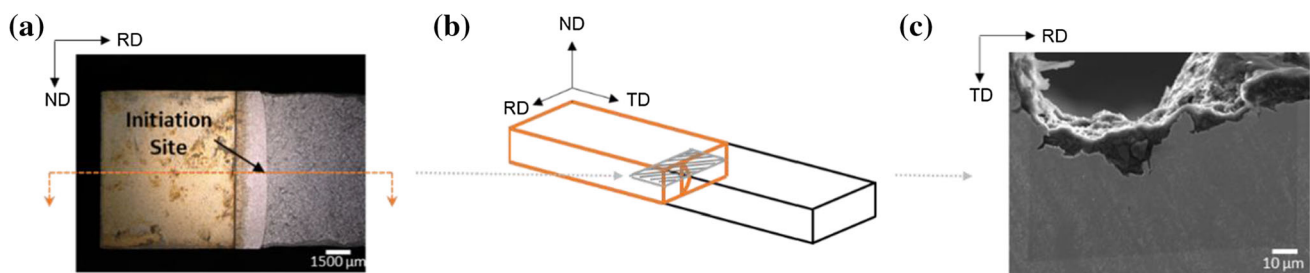


Figure 3 Schematics of the T-L sample preparation for fractographic profile investigation showing (a) the sample's distance ground to analyse the crack propagation path in an area

fractured in triaxial stress state, (b) an illustration of the specimen's plane which was metallographically prepared, and (c) the polished fracture profile.

650 SAM, equipped with a cylindrical mirror analyser (CMA) and operated with an energy resolution $\Delta E/E$ of 0.6%, was used. An electron beam of 5 kV and 150 nA at an angle of incidence of 30° with respect to the sample surface normal was applied. At these experimental conditions, the lateral resolution was approximately 0.3–0.4 μm , and the low pressure in the main chamber was about 7×10^{-8} Pa. Each line scan, consisting of 256 scan points for the elements C, Mn, Cr, Mo, P, Ni and Si, was made through intergranular facets of the specimen, crossing the grain boundaries. These elements were selected for this analysis, as they were identified to be enriched in the segregation bands or for being frequently reported in the literature as the main elements responsible for grain boundary embrittlement in steels, such as P including the case of temper embrittlement in the references [11, 33–35].

Results and discussion

Three variables were analysed in the CTOD tests: thickness position, notch orientation, and crack tip constraint. SENB specimens were extracted from the top and middle sections of the S690QL steel plate and the notches were machined in T–L and L–T orientations. Initially, two notch depths were considered to investigate the constraint (crack depth) effects: $a/W = 0.5$ and 0.1. These different notch depths allowed the analysis of high- and low-constraint conditions, respectively. Figure 4 presents the failure probability as a function of CTOD for the top and middle sections, in T–L and L–T orientations and $a/W = 0.5$ and 0.1. Note that sub-sized SENB specimens were proven to be suitable only for cleavage-controlled fractured specimens, meaning that valid CTOD values should be below 0.2 mm [36]. Hence, specimens with CTOD values greater than 0.2 mm,

presenting extensive plastic deformation, as confirmed by visual inspection, were disregarded in the following discussions made in this study.

Effect of notch orientation and constraint

As can be seen in Fig. 4, most of the top, low-constraint specimens, in both notch orientations, present CTOD values higher than 0.2 mm and show mixed-mode fracture characteristics. These specimens represent more than 50% of the tested specimens in this condition. Thus, the a/W ratio of 0.1 does not provide representative CTOD results for further discussion of cleavage fracture in the top section. However, the effect of notch orientation can be investigated for the high-constraint and low-constraint middle specimens. Moreover, no significant difference in the CTOD values between T–L and L–T orientations was observed either for the top or middle. This behaviour is expected since the S690QL plate does not have a preferential crystallographic orientation–texture–through the thickness [11]. Therefore, the material is considered isotropic in-plane.

As many of the low-constraint tests were not valid and, therefore, not included in the analysis (most of the specimens in the top position with an a/W ratio of 0.1 present critical CTOD values greater than 0.2 mm), a mid-constraint ($a/W = 0.25$) condition was included in the test matrix. As the notch orientation does not play a role, the CTOD results (Fig. 4) for T–L and L–T orientations were added up for the high- and low-constraint conditions ($a/W = 0.5$ and 0.1), and mid-constraint specimens ($a/W = 0.25$) were only tested in T–L orientation.

Figure 5a shows the failure probability as a function of CTOD for the top and middle sections and $a/W = 0.5, 0.25$, and 0.1. Figure 5b shows the relationship between the average CTOD values and the a/W ratio for the top and middle sections. On the one

Figure 4 Rank failure probability versus CTOD of the experimental fracture tests at -100°C , top and middle sections, T–L and L–T orientations, and $a/W = 0.5$ and 0.1.

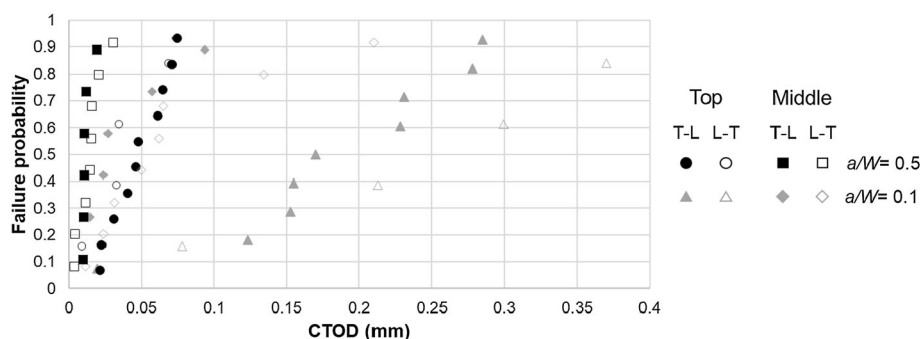
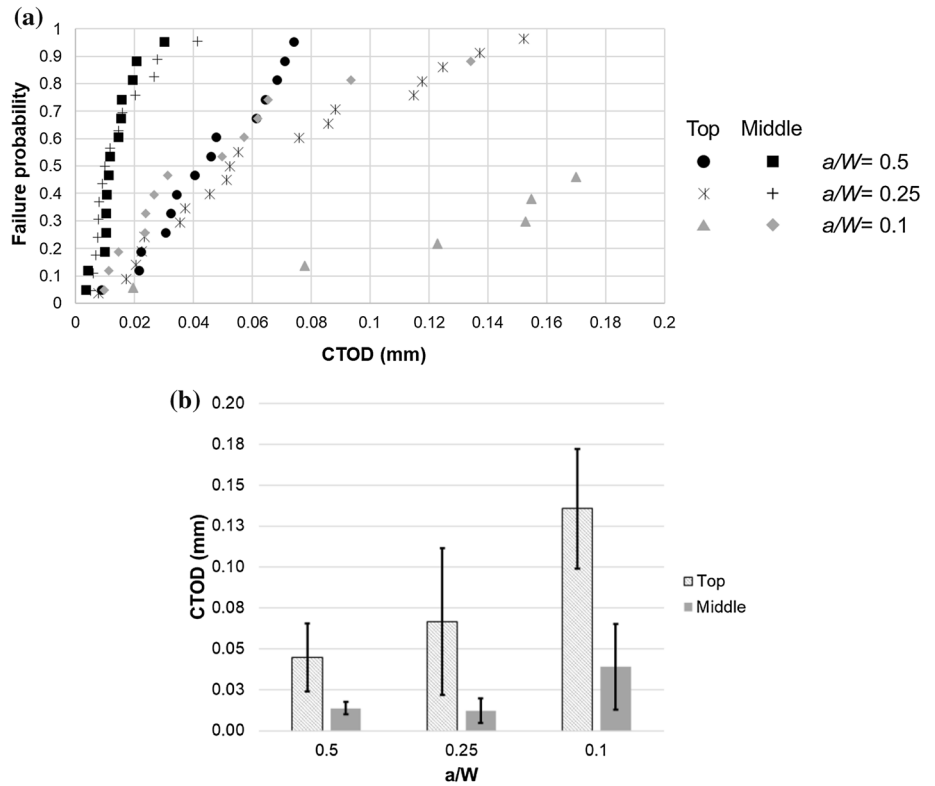


Figure 5 Experimental CTOD data presented as **(a)** rank failure probability and **(b)** average values and standard deviation from the average for the top and middle sections and $a/W = 0.5, 0.25,$ and 0.1 . The data includes the combined T–L and L–T CTOD results for $a/W = 0.5$ and 0.1 , and T–L CTOD for $a/W = 0.25$.



hand, a considerable increase in CTOD values with the crack depth reduction is seen for the top section, primarily for the $a/W = 0.1$ condition. On the other hand, the a/W influence on CTOD is minor for the middle section, even for $a/W = 0.1$.

In general, the lower the a/W ratio, the larger the CTOD [10, 26, 27]. This correlation is associated with the specimen's plastic zone and the resultant stress state ahead of the crack tip when varying the crack depth. Sorem, Dodds, and Rolfe [10, 26] performed studies comparing the behaviour of shallow- and deep-cracked CTOD specimens of A36 steel. The authors observed that, when the material is in a linear-elastic regime (e.g. the lower shelf of the ductile–brittle transition curve, where the material failure is controlled by cleavage), shallow and deep-cracked specimens present the same stress ahead of the crack tip for the same CTOD value. In other words, fracture toughness is independent of a/W values. On the other hand, in the elastic–plastic regime, at the same CTOD level, stresses vary ahead of the crack tip for shallow- and deep-cracked specimens. Furthermore, they [10] observed that when a CTOD specimen with $a/W = 0.05$ or 0.1 is loaded, the plastic zone ahead of the crack tip interacts with the nearest free surface before a plastic hinge forms, which would cause the

specimen to be invalid. For the investigated level of loading, the authors observed that at $a/W = 0.15$, the formation of a plastic hinge coincides with the interaction of the plastic zone with the nearest specimen's free surface. At $a/W = 0.2$, the plastic hinge developed long before the plastic zone interacted with the free surface. Finally, at $a/W = 0.5$, the plastic zone was limited to a small region ahead of the crack tip without expanding to the free surface. Hence, for the A36 steel, the boundary between shallow and deep cracks was found to be around $a/W = 0.15$. However, this number may vary with the loading, specimen size, and material hardening behaviour. For instance, materials that have a considerable strain hardening may have larger a/W transition values as the hardening expands the plastic zone to the free surface [26]. Hence, although the shallow- and deep-cracked specimens are submitted to the same loading conditions and, consequently, would present similar stress levels ahead of the crack tip, the expanded plastic zone in shallow-cracked specimens relieves the stress, reducing the triaxiality, and also the constraint. Then, shallow-cracked specimens need to be deformed further to reach the critical stress for failure, leading to a larger CTOD [26]. This resultant larger strains experienced by the low-constraint

specimens before fracture may involve the crack tip blunting [26].

To simulate the stress distribution near the crack tip (Fig. 6) for $a/W = 0.5, 0.25,$ and 0.1 , a finite element analysis (FEA) is performed in Abaqus 2017. The specimen is modelled as a 3D deformable solid with 20-noded hexahedral elements. The supports and load roller are modelled as frictionless rigid surfaces. The initial pre-fatigued crack tip is modelled as a finite notch that is 0.005 mm in radius with the smallest element having the dimensions $0.001 \times 0.005 \times 0.067$ mm³. A full Newton–Raphson algorithm is used to solve the geometric and material nonlinearity in an implicit method. The stress–strain relationship of the steel is characterised by Ludwik’s law, defined with the flow stress (σ) and the effective plastic strain (ε_p) as:

$$\sigma = \sigma_y + K\varepsilon_p^{n_L} \quad (3)$$

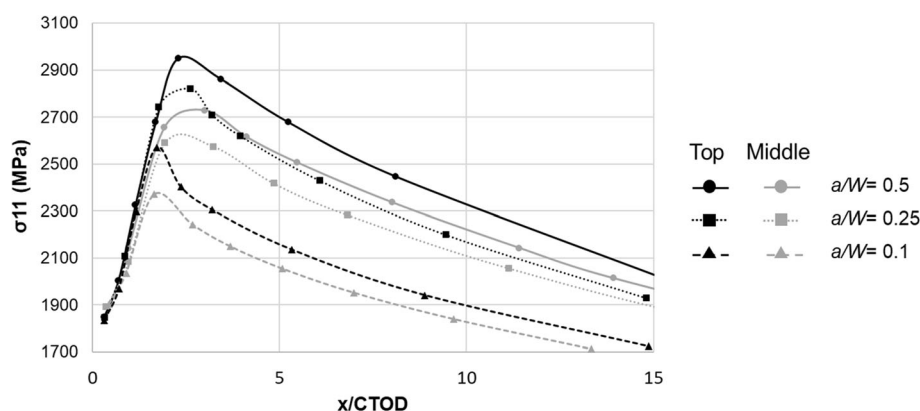
where σ_y is yield strength and K and n_L are material parameters fitted from tensile tests.

The experimental tensile true stress–strain curves and the fitting curves with Eq. 3 for the top and middle sections (tensile test curves are plotted until the maximum stress) are presented in our previous work [32]. Figure 6 displays the normal stress distribution in front of the crack tip for the top and middle sections and the three tested a/W , $0.5, 0.25,$ and 0.1 . The figure corresponds to CTOD = 0.05 mm for all the cases. It can be seen that, for both top and middle sections, a smaller a/W ratio implies a lower normal stress ahead of the crack. This explains the very different CTOD values between high- and low-constraint conditions observed for the top section at -100 °C. However, for the middle section, such a difference is not observed. Moreover, the normal stress

in the top section is higher than in the middle section for the same a/W ratio due to the difference in yield strength. However, the middle section still exhibits lower fracture toughness than the top section.

The weak dependence of the fracture toughness on the a/W ratio in the middle section relative to the top may be explained by the ductile-to-brittle transition behaviour. First, for shallow-cracked specimens, the material experiences fracture at a different temperature relative to the reference temperature (T_0) because constraint is known to affect the ductile–brittle transition temperature [27]. Shallow-cracked specimens need more deformation to reach the local fracture stress to fail, resulting in a larger CTOD. It means that the transition for low-constraint specimens occurs at a lower temperature than for high-constraint specimens [27]. Hence, at the same test temperature, the material under different constraints may be tested in different regimes of the ductile-to-brittle transition curve. Second, for each thickness section, T_0 was calculated based on the master curve method using the ASTM E1921 [37]. For the top and middle sections, T_0 is -101 °C and -41 °C, respectively. It means that, at the test temperature (-100 °C), the fracture behaviour of the top section is being assessed near T_0 and closer to the ductile-to-brittle transition. On the other hand, for the middle section, the test temperature (-100 °C) is 60 °C further from T_0 . Therefore, the toughness of the middle section is assessed near or at the lower shelf due to its embrittled microstructure, as discussed in [11]. In this case, even with the shift of the ductile–brittle transition curve for the shallow-cracked specimens, the middle section remains at the lower transition part of the ductile–brittle transition curve, where less plasticity is involved. The top section, in turn, is nearer the upper part of the transition.

Figure 6 Normal stress (σ_{11}) at the specimens’ mid-plane and distance x mm from the crack tip (undeformed configuration).



Hence, the fracture toughness differences between $a/W = 0.5$ and 0.1 in the middle section are smaller than for the top section.

The different behaviour between the top and middle sections in low-constraint conditions may be explained by fracture surface analysis. The fracture surface of low-constraint specimens shows that different damage characteristics for top and middle samples may occur even having the same initiation site type, an Nb-rich inclusion. Figure 7a shows that for the top section, the fatigue pre-crack is followed by a stretch zone—characteristic of plastic deformation as a consequence of crack tip blunting—and a flat transgranular cleavage surface (mixed-mode fracture usually observed in the ductile-to-brittle transition region of the ductile–brittle curve, but still represents a cleavage-controlled fracture). As previously explained, the lack of constraint causes the material to experience larger deformation to compensate for stress relief. Then, the crack blunts before reaching the critical stress to failure, resulting in a stretch zone just after the pre-fatigue crack tip and before the

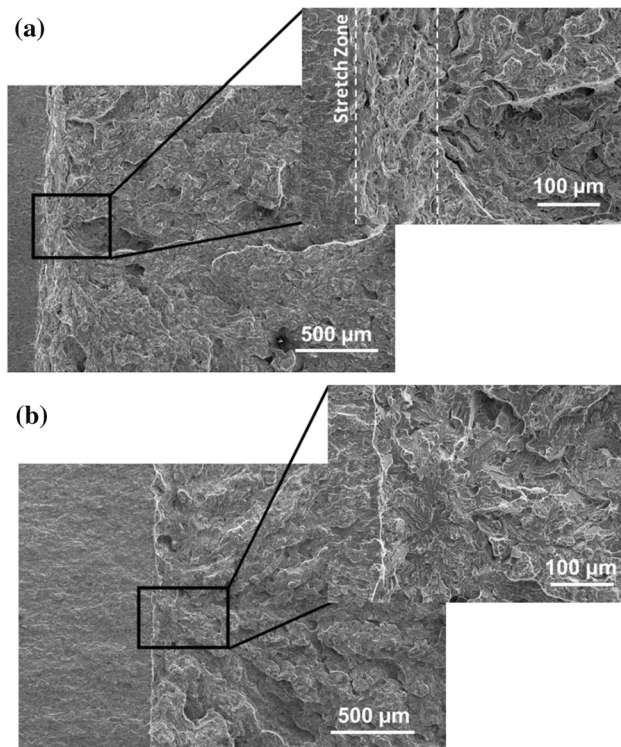


Figure 7 SEM micrographs of fracture surfaces of low-constraint specimens ($a/W = 0.1$) tested at $-100\text{ }^{\circ}\text{C}$ from (a) top, with a critical CTOD of 0.12 mm showing a fatigue pre-crack, stretch zone, and cleavage area, and (b) middle, with a critical CTOD of 0.02 mm showing a fatigue pre-crack and cleavage area.

cleavage surface. For the same constraint condition, the fracture surface of middle specimens either does not show any or presents only a small stretch zone compared to the top, as shown in Fig. 7b, reflecting the limited crack tip plasticity resultant from the detrimentally brittle microstructure. The presence of the stretch zone and its width may be related to the type of initiation site and its distance far from the pre-crack tip.

Microstructural factors controlling cleavage crack initiation

Figure 8b shows the average CTOD and the standard deviation from the average for all analysed constraint conditions. The distinct difference in fracture toughness between the top and middle sections is notable, where the top shows the highest CTOD values. The adverse microstructure of the middle section in thick-section steel plates in terms of fracture behaviour was already pointed out before [5, 6, 12, 14, 29], including for the high-strength steel investigated in this study [11]. According to Bertolo et al. [11], the unfavourable microstructure of the middle section compared to the top section of the 80-mm-thick quenched and tempered S690QL steel plate includes “larger prior austenite grain sizes, larger sizes and area fraction of inclusions, the presence of defects associated with the circular and cubic inclusions and with their interface with the matrix, clusters of cubic inclusions that may also be distributed along the PAG boundaries, and the long interfaces with the largest hardness gradients”. To investigate which microstructural features are involved in the cleavage initiation responsible for the difference in fracture behaviour, the CTOD fracture surfaces were analysed by SEM based on the river lines that lead to the initiation site.

Fracture surfaces of 32 single edge-notched bending (SENB) specimens tested at $-100\text{ }^{\circ}\text{C}$ including high- and low-constraint conditions ($a/W = 0.5$ and 0.1 , respectively), and T–L and L–T orientations extracted from the top and middle sections of the plate were investigated. In 63% of all surfaces, it was possible to identify microstructural features triggering the fracture. In the other 37% of samples, it was not possible to identify the initiation site because fracture surfaces did not show clear river lines or the river lines did not converge.

Figure 8a shows the number fraction of each type of initiation site that was observed in the top and

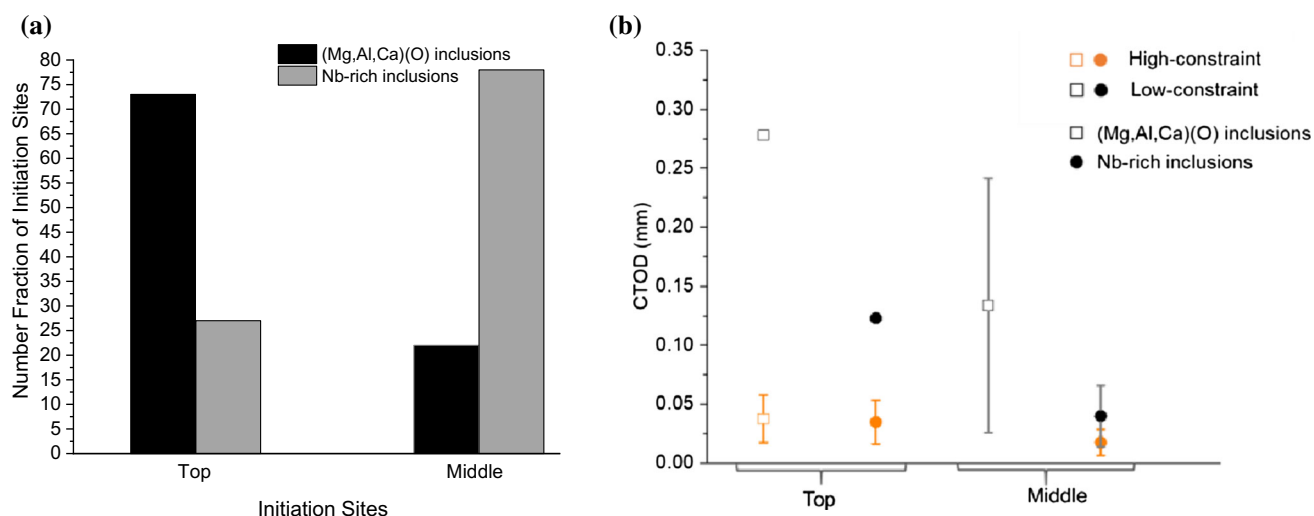


Figure 8 Summary of the fracture surface analysis and CTOD tests showing the (a) number fraction of each type of initiation sites that were observed in specimens from the top and middle section, with no distinction between T–L and L–T, and high- and

middle section, with no distinction between notch orientation and constraint. For the top section, initiation sites were identified for 11 fracture surfaces, 9 from high-constraint and 2 from low-constraint samples. The (Mg, Al, Ca)(O, S) inclusions, which in some cases also include traces of Ti, B, C, and N, are the most common initiation sites, being present in 73% of the identified cases (7 high-constraint and 1 low-constraint). The remaining 27% of the specimens had their fracture process triggered by Nb-rich inclusions (2 high-constraint and 1 low-constraint). Within the 27%, more than 2/3 presented the lowest CTOD values of their categories (constraint and orientation conditions) showing a more detrimental effect of Nb-rich than of oxide inclusions, as shown in Fig. 8b. Hence, cleavage initiation from Nb-rich inclusions represents the worst-case scenario. Note that the points without a scatter bar refer to initiation sites observed in only one specimen. Figure 9 shows an example of a fracture surface where an (Mg, Al, Ti)(O, C, N) inclusion was observed to be a cleavage initiation site in a high-constraint, top quarter, L–T specimen.

In specimens extracted from the middle section of the plate, initiation sites were identified for 9 fracture surfaces, 3 from high-constraint and 6 from low-constraint. The Nb-rich inclusions were observed to be responsible for triggering the fracture process in 78% of the identified cases (3 high-constraint and 4

low-constraint specimens and **b** the CTOD values for high- and low-constraint specimens (represented in orange and black colours, respectively) varying the type of initiation site. The points without a scatter bar refer to initiation sites observed in only one specimen.

low-constraint), even though oxides are the majority, 76% (Table 3). This is likely to be mainly attributed to the larger sizes and clustering of Nb-rich inclusions. These inclusions were found in the initiation site both single and distributed as clusters. Additionally, oxides were observed in 22% of the identified initiation sites (2 low-constraint) which had the highest CTOD values within their categories (constraint and orientation condition). Figure 10 shows an example of a fracture surface of a low-constraint, middle, T–L specimen where an Nb-inclusion can be recognised as a cleavage initiator.

The detrimental effect of Nb-rich inclusions can be explained by the microstructural observations reported by Bertolo et al. for this S690QL steel [11]. First, compared to the oxide inclusions, Nb-rich inclusions tend to be larger and distributed in clusters. When distributed as clusters, Nb-rich inclusions may be considered as a single larger inclusion due to their proximity, through which the cluster represents an easy propagation path. As both inclusion types were observed acting as crack initiators, it indicates that the initial crack length in the fracture process is the size of these inclusions. According to Griffith's theory [38], the larger the crack, the lower the fracture stress. Hence, Nb-rich inclusions represent the weakest microstructural link for fracture. Lastly, cubic-shaped inclusions, as a result of their sharp edges, present larger residual stresses in the interface

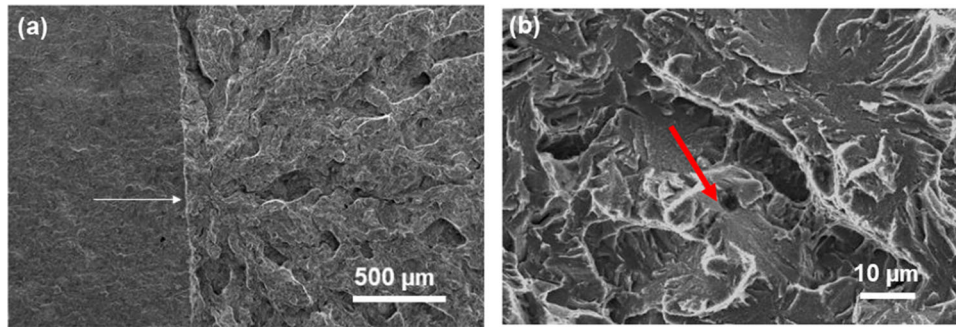


Figure 9 SEM micrographs showing (a) river lines and a white arrow indicating the cleavage initiation site in high-constraint, top, L–T specimen fractured at $-100\text{ }^{\circ}\text{C}$ with CTOD equal to 0.01 mm

and (b) an (Mg, Al,Ti)(O, C, N) inclusion (indicated by the red arrow) as a likely initiation site.

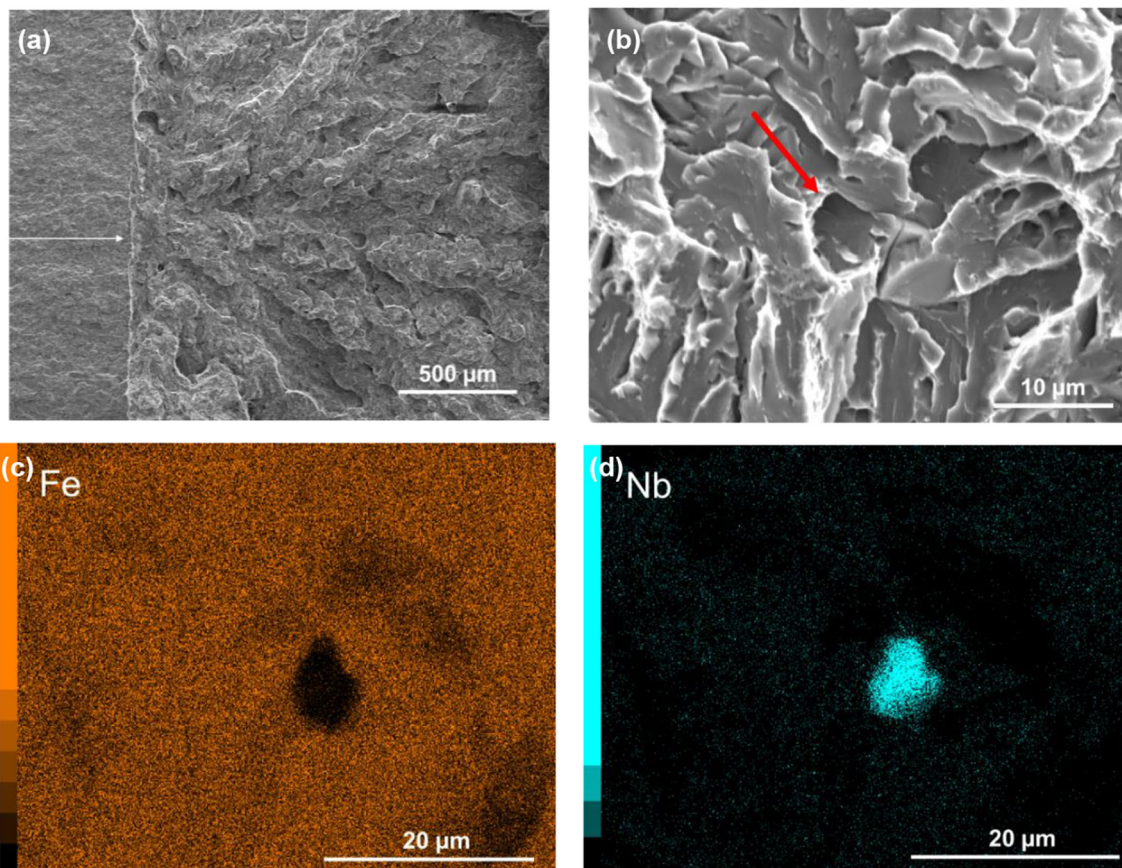


Figure 10 SEM micrographs and EDS mapping showing (a) river lines and a white arrow indicating the cleavage initiation site in low-constraint, middle, T–L specimen fractured at $-100\text{ }^{\circ}\text{C}$ with CTOD equal to 0.015 mm and (b) an Nb-rich inclusion (indicated

by the red arrow) located in the cleavage initiation site (c and d EDS mapping of Fig. 10b showing Fe and Nb maps, respectively, for the matrix and Nb-rich inclusion).

with the steel matrix originated from the steel processing and act as stress concentrators, raising stress more effectively than circular inclusions [39]. Along with the intrinsic detrimental effect of Nb-rich inclusions, the pre-existence of cracks in the

inclusions themselves and in the interface inclusion/matrix, most often for the Nb-rich inclusions, may also explain the lower fracture toughness in the middle section. Nucleation in a hard particle and the unstable crack propagation across the particle/matrix

interface and the matrix are the steps of cleavage fracture [3]. However, the existing crack associated with these inclusions may serve as a Griffith crack. Hence, the crack propagation into the matrix is the only likely remaining stage in the fracture process in the middle section, while in the top section, both nucleation and propagation are necessary for fracture to occur.

Microstructural factors affecting cleavage crack propagation

In general, cleavage crack propagation mode is transgranular and is governed by crystallographic microstructural characteristics [3, 40–42]. For instance, the cleavage crack path is affected by high-angle grain boundaries (e.g. prior austenite, packet, and block boundaries) and cracks preferentially propagate through planes with the lowest surface energy, {001} and {011} [42]. According to Morris [40], in cleavage fracture, the laths inside a block share the same cleavage plane and cleavage as a unit. This is expected as lath boundaries are low-angle grain boundaries and, therefore, not able to deflect the crack. Therefore, laths are ineffective in deflecting or hindering a cleavage crack and are not the focus of this work. Furthermore, the complex crystallographic structure of lath martensite and lath bainite is observed to influence the local changes in the crack path [40, 41, 43]. Hence, the transverse section of CTOD fracture surfaces was analysed by EBSD to investigate the correlation between crack propagation path and microstructural crystallographic features, and, therefore, establish the mechanism of failure of the S690QL high-strength steel. Figures 11 and 12 show the inverse pole figures (IPF), kernel average misorientation (KAM) maps of the fracture surface profile, and individual prior austenite grains involved in the propagation process for the specimens extracted from the top and middle thickness position in T–L orientation, respectively.

It can be seen that the cleavage crack propagation micromechanism is transgranular, where the crack propagates through the prior austenite grains. Along the propagation path, it is clear that the IPF presents dense zones of poorly indexed points. As a dislocation-pileup-driven process, cleavage is preceded by microplasticity [3]. Hence, the poorly indexed points might be associated with plastic deformation during the fracture process. The KAM, obtained via EBSD

data, is a measure of the average misorientation angle between a central point and all points at the perimeter (its neighbours) and it has been reported to be dependent on the geometrically necessary dislocations (GND) density [44]. Consequently, it is frequently used as a measure of plastic deformation. Figures 11b and 12b are KAM maps for the 3rd neighbour. By comparing the IPF and KAM maps (Figs. 11a with b and 12a with b), it can be seen that the KAM areas with maximum misorientation (red) match with the IPF areas with poor indexation. Thus, plastic deformation is involved in the cleavage fracture process leading to a significant density of dislocations and, consequently, to a poor indexation of points in EBSD maps in the subsurface of the fracture plane. Nevertheless, these specific areas do not provide accurate and reliable data for analysis of the propagation micromechanism and, consequently, are not considered in further discussion.

The 3D crystal lattice cubes in Figs. 11a and 12a indicate the crystal orientations of the grain substructures directly below the fracture surface. Green, red and blue circles are used to, respectively, highlight when {100}, {110} and {310} plane traces under the fracture surface are aligned parallel (tolerance misorientation of 10°) to the fracture plane. For almost the entire analysed length (around 95%) of the fracture surface, the cleavage crack propagates through the {100} and {110} planes in the top and middle sections, where both families of planes have a similar contribution. Less than 10% of the cleavage planes seem to be aligned to the {310} planes, also observed to be involved in the cleavage process of other bcc steel [45]. Hence, the most favourable cleavage planes in the S690QL steel under study are the {110} and {001} planes.

The contribution of crystallographic grain structures in crack propagation is also acknowledged in the literature [40, 41, 46]. However, there is no consensus on cleavage crack propagation mechanisms across PAG in tempered lath martensite and lath bainite. Ideally, in lath microstructures, individual PAG are divided into four distinguishable packets that share the same planes of the parent austenite. In other words, they have the same Kurdjumov–Sachs (K–S) variant (according to Bertolo et al. [11], this steel has a K–S crystallographic relation to the parent austenite). Each packet is composed of three blocks of different Bain variants [40]. Hence, Bain (Figs. 11 and 12c and e) and K–S (Figs. 11 and 12d and f) variant

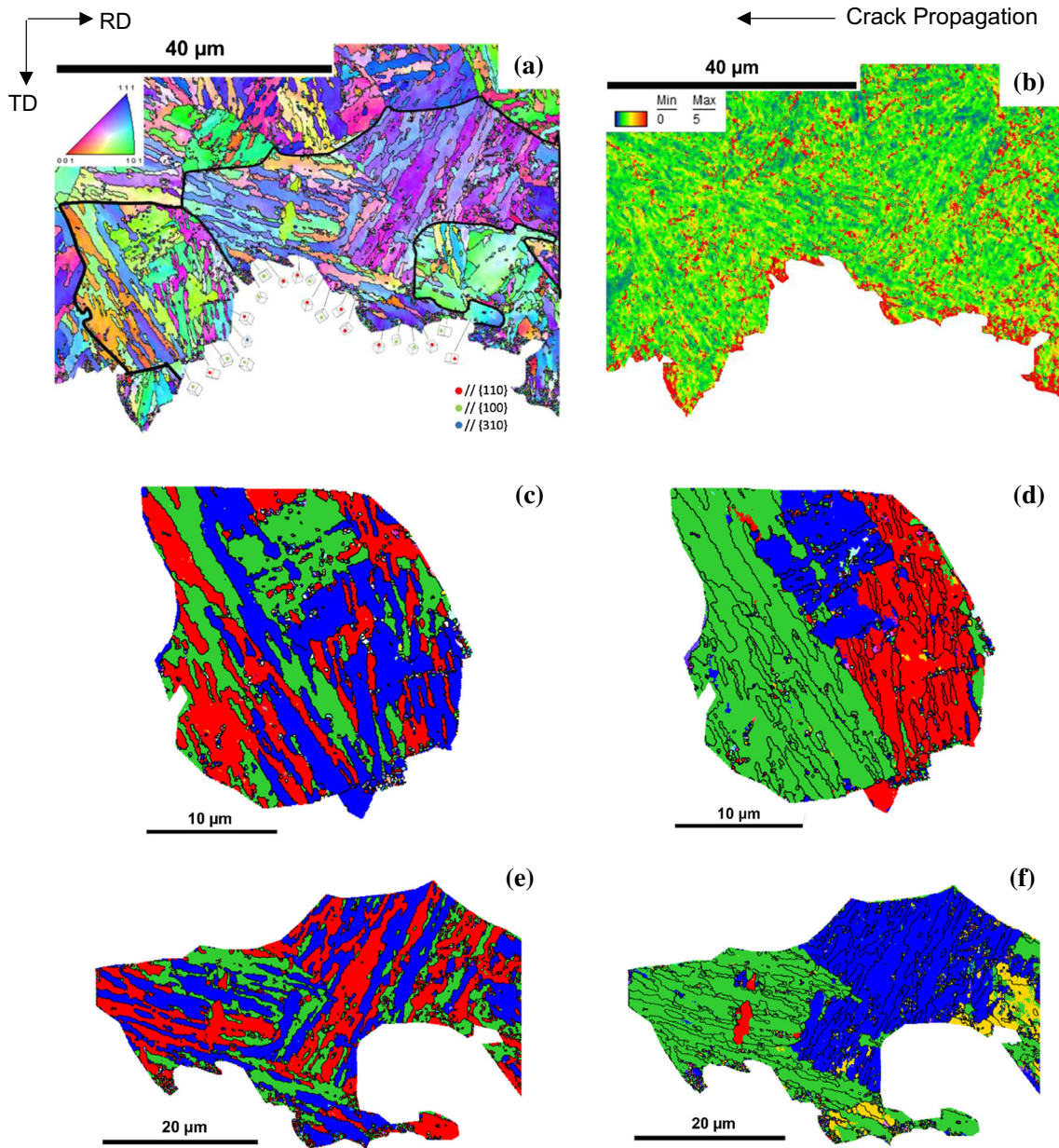


Figure 11 Fractographic profile of a CTOD specimen extracted from the top, high-constraint, T–L presented as **(a)** Inverse Pole Figure, **(b)** Kernel Average Misorientation map, **(c)** and **(d)** are an individual PAG located at the left-hand side of **(a)**, **(e)** and **(f)** are individual PAG located at the right-hand side of **(a)**. The colours in

(c) and **(e)** represent different Bain variants, while the colours in **(d)** and **(f)** represent the different K-S variants). Thin black lines are high-angle ($> 15^\circ$) grain boundaries and the thick black contour in **(a)** is the PAG boundary.

maps were generated for individual PAG grains of top and middle sections, where different colours correspond to different Bain or K-S groups. In general, it can be seen that the PAG grains follow the previously explained ideal hierarchical lath structure: each PAG has four packets and each of them has three Bain variants. In the cases where there are not four packets, it can be the case that another packet is

part of the other half of the fracture surface. When the packet does not contain three Bain variants, it might be that the packet is relatively small.

In both top and middle thickness positions, the crack is observed to significantly deflect from its path in PAG, packets, and block boundaries mostly where the neighbouring sub-structure has a different Bain axis. However, in a few boundaries with different

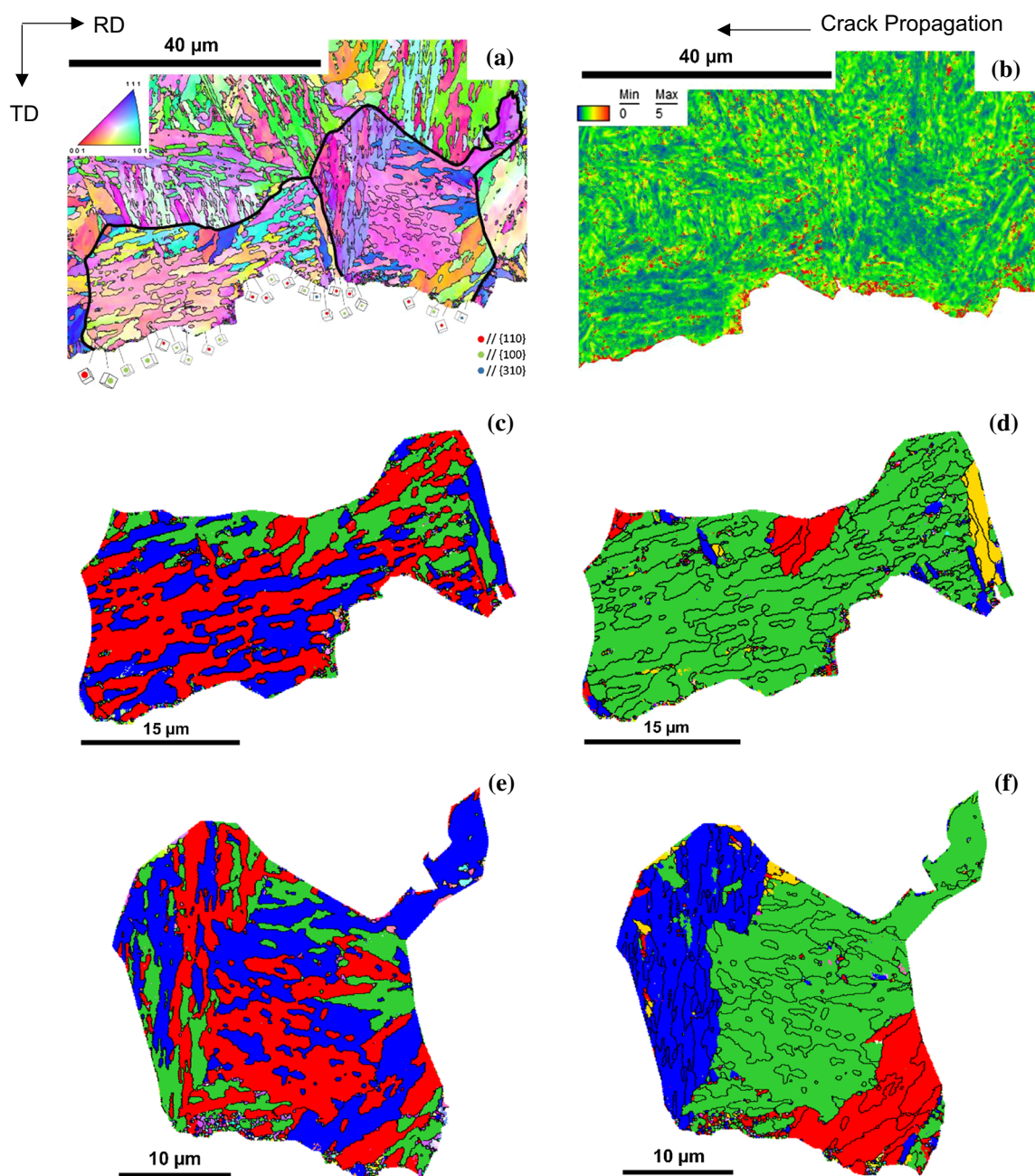


Figure 12 Fractographic profile of a CTOD specimen extracted from the middle, high-constraint, T–L presented as (a) Inverse Pole Figure, (b) Kernel Average Misorientation map, (c) and (d) are individual PAG located at the left-hand side of (a), (e) and (f) are individual PAG located at the right-hand side of (a). The colours in

(c) and (e) represent different Bain variants, while the colours in (d) and (f) represent the different K-S variants). Thin black lines are high-angle ($> 15^\circ$) grain boundaries, and the thick black contour in (a) is the PAG boundary.

Bain axis of the middle section, only slight deflections were observed. This could be attributed to the thickness of the Bain area, as also observed by Wang et al. [41]. It is also important to mention that some areas could not be analysed as only a small remaining part of the other specimen's half was present not

leading to a clear and reliable conclusion. Thus, the investigation of the transverse section of the fracture surfaces shows that despite the differences/classification of sub-structures into PAG, packets, and block boundaries, the Bain zone is the effective crystallographic microstructural characteristic in deflecting

the cleavage crack. This is in agreement with what was found for heat affected zones of an offshore engineering steel tested by Charpy [41].

Although one of the characteristics of cleavage fracture is the transgranular mode, 36% of the studied fracture surfaces presented zones of intergranular fracture. The intergranular fracture was observed locally in some samples, while in others these regions extended over a significant part of the fracture surface. Figure 13 shows SEM micrographs of a fracture surface with extensive intergranular fracture and EDS maps along this area. It should be noted that this extensive intergranular fracture region does not start from the initiation site, which is shown in the insert image 1 of Fig. 13. Hence, the intergranular fracture is mainly affecting the propagation micromechanism. In image 1, it is possible to observe the presence of cleavage facets and Nb-rich inclusions, responsible for triggering fracture. Ahead of this area, in image 2, the region of intergranular fracture begins, which resembles a corridor-like path composed of smooth facets that are arranged in a straight line, in the presence of Nb-rich inclusions. From this area, it is possible to observe the presence of several Nb-rich inclusions decorating the grain boundaries which are directly related to the grain boundary embrittlement and lead to unexpected intergranular fracture.

Like in the specimen analysed in Fig. 13, some other samples showed characteristics of intergranular

fracture where Nb-rich inclusions were not present or distributed throughout the region along PAG boundaries. It means that, in some regions, the intergranular fracture was not associated with these particles. Therefore, it may be that there is an additional microstructural contribution to the grain boundary embrittlement in the central part of the plate, such as the segregation of alloying elements.

For several years, researchers have been studying the effect of alloying segregation in the boundaries of PAG. Many authors report that, along with the inclusions and precipitates, the segregation of elements along the PAG boundaries can reduce the boundary cohesion, embrittling them and, consequently, making them prone to intergranular fracture [33, 47]. This segregation can take place during casting, which gives rise to segregation bands in the centre of steel plates. Elements such as Mo, C, Mn, Cr, Si, Ni were observed to segregate in the middle section of the S690QL steel studied herein, and their content was quantified by EPMA [11]. P is acknowledged as a significant embrittling element in steel, especially if Si and Mn, which are often responsible for reducing the cohesion of grain boundaries, are present in high content [35, 48, 49]. Unfortunately, the degree of segregation of P in the segregation bands cannot be analysed by EPMA due to the low P concentration in the S690QL steel (0.009 wt%), as the EPMA detection limit is equal to 0.1 wt%. However,

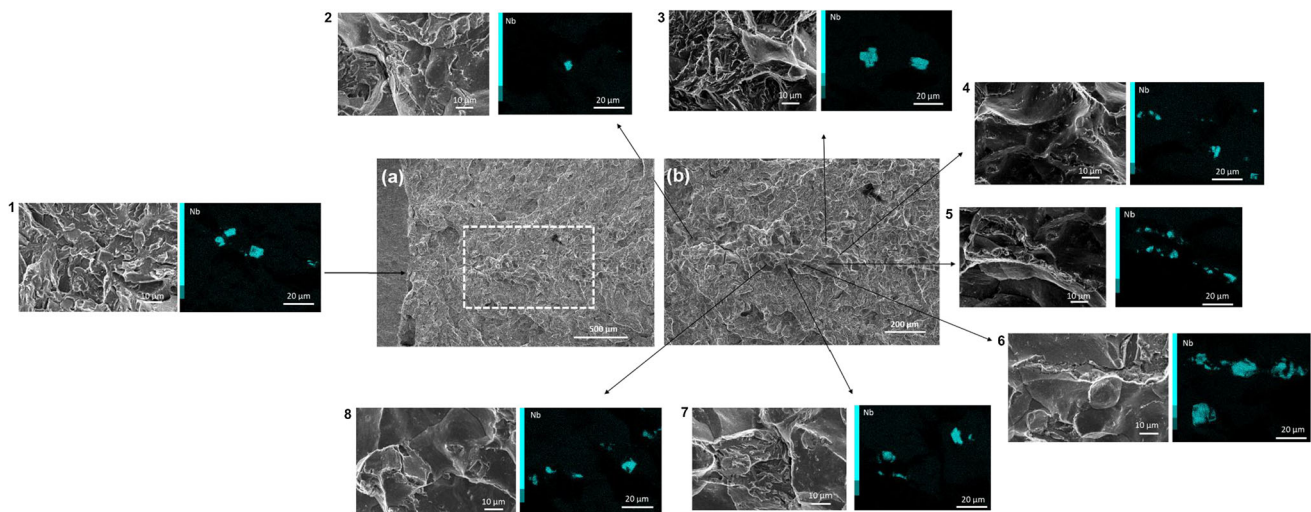


Figure 13 SEM micrographs of the fracture surface in a low-constraint, middle, T–L specimen fractured at $-100\text{ }^{\circ}\text{C}$ with CTOD equal to 0.03 mm showing (a) river lines indicating the cleavage initiation site and a linear zone of intergranular fracture (inside the dashed rectangle) and **b** higher-magnification image of

the area highlighted by the white rectangle in (a). SEM images and Nb EDS maps numbered from 1 to 8 show, in greater magnification, areas of (a) and (b) such as the cleavage initiation site and areas along the line of intergranular fracture where Nb-rich inclusions were observed.

the segregation of P should not be ruled out. Mn and Si were also observed to segregate in the bands of the middle section and are highly likely elements responsible for embrittling the PAG boundaries. Thus, for a more precise and detailed understanding of the grain boundary embrittlement due to the alloying segregation, Auger Electron Spectroscopy analyses (AES) are required. AES is the most used technique in the study of element segregation in the grain boundaries on fracture surfaces [50, 51].

Figure 14 shows an SEM micrograph of a large region, including areas 3, 4, 5, and 6 of Fig. 13, that fractured in an intergranular manner in a CTOD specimen from the middle section. The location of Nb-rich inclusions in these areas is also shown. The line scan results via AES are presented in Fig. 15. An intergranular fracture surface is known for its shiny and flat surface, and straight edges of the grain (grain boundaries). As prior austenite grains have different orientations, the facets aligned in different angles to the normal direction make the grain boundaries distinguishable from the SEM image and they can be located along the Auger line scan. The great majority

of the peaks of all elements are located in the prior austenite grain boundaries present in the intergranular areas. Hence, these boundaries are enriched with C, Cr, Mn, Mo, Si, P, and Ni. However, the elemental spectrum shows that part of the line scans that cross transgranular areas also shows peaks of the previously mentioned elements. This observation suggests that the degree of grain boundary segregation may be not sufficient in certain areas to individually cause grain boundary embrittlement and lead the crack to propagate through the grain boundaries. These areas are probably located in the segregation bands due to the presence of the main segregated elements according to the EPMA analysis [11]. One possible explanation for this behaviour is a competition between elements that increase the grain boundary cohesion, such as C, and elements that reduce the grain boundary cohesion, such as Mn, and P [33, 52]. Therefore, the presence of Nb-rich inclusions decorating the PAG boundaries is a necessary condition to sufficiently weaken the grain boundaries for the intergranular fracture to occur in areas where the

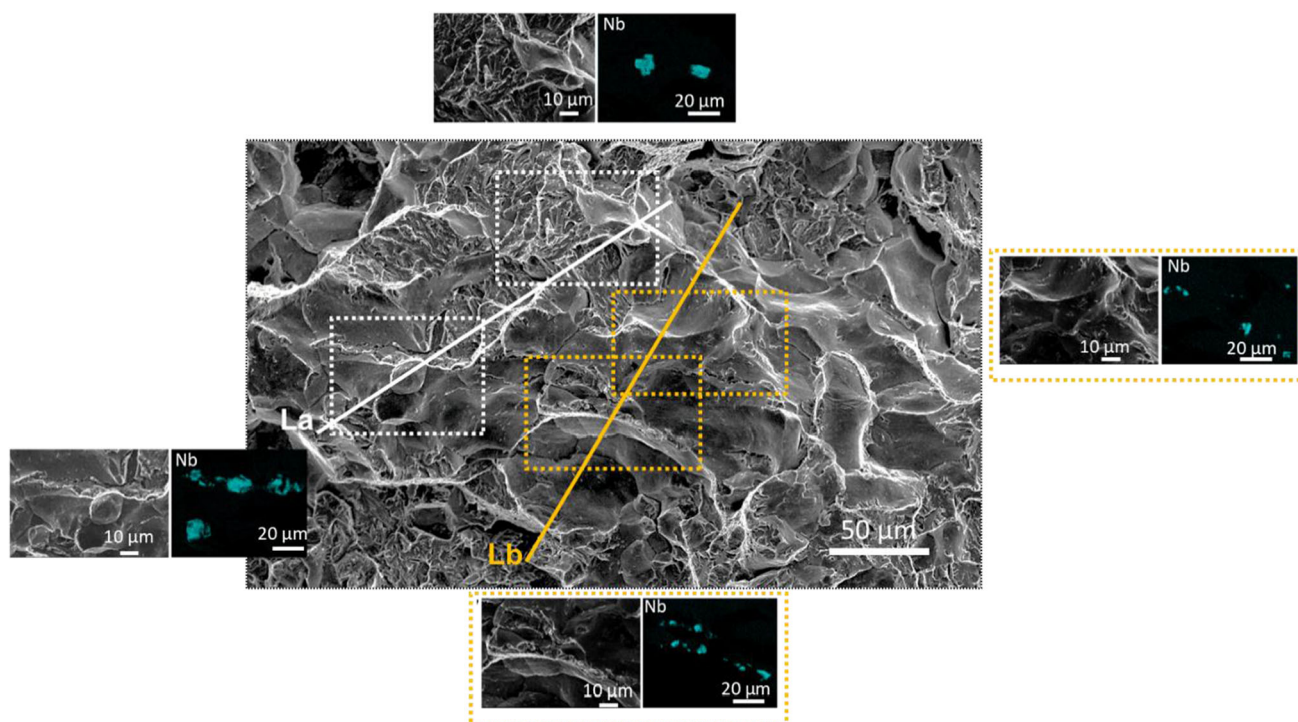


Figure 14 SEM micrographs showing the line scans, La and Lb, measured by SAM as well as the locations of Nb-rich inclusions along this selected intergranular fracture area.

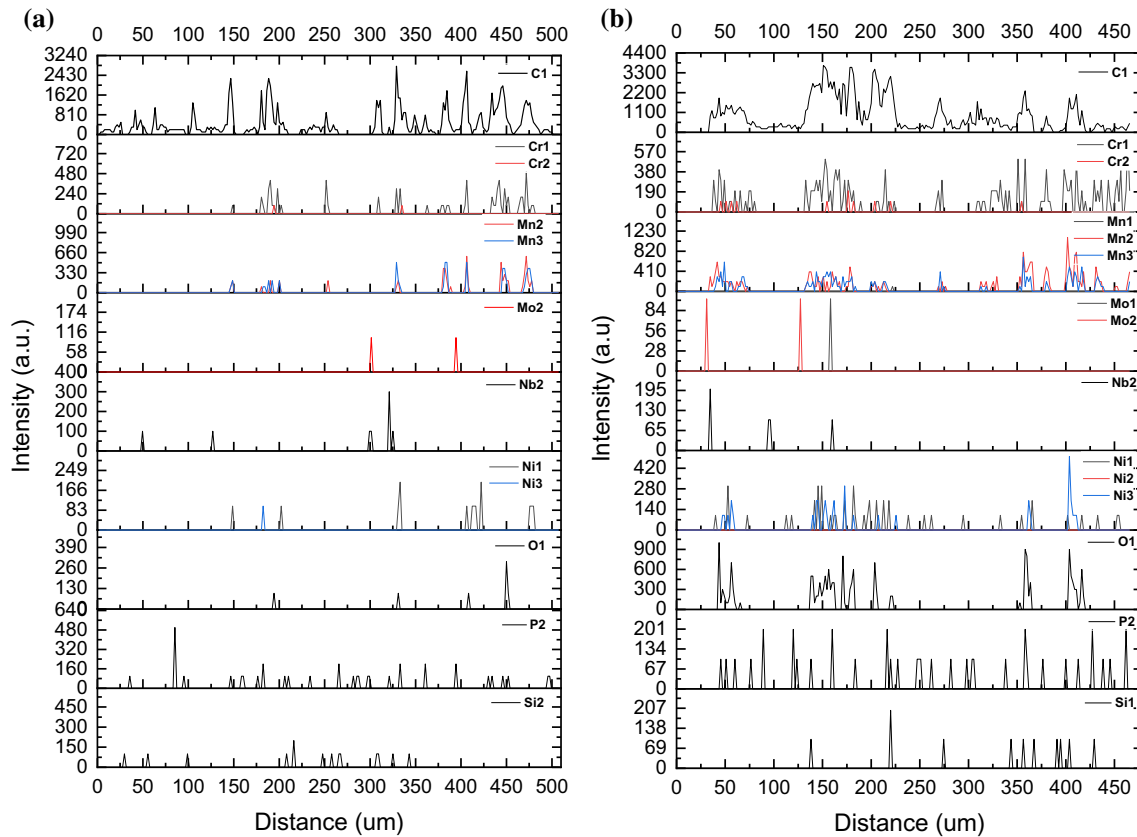


Figure 15 Elemental spectrum results from the scanning auger microprobe line scan analysis for (a) line a and (b) line b identified in Fig. 14.

grain boundaries are not sufficiently weakened by the elemental segregation.

Conclusions

The studied thick-section S690QL high-strength steel presents through-thickness microstructural variations. In general, larger size and area fraction of inclusions as well as larger PAG sizes are found in the middle section compared to the top. Additionally, Nb-rich cubic inclusions, observed in higher densities in the middle section, are often distributed as clusters and may be found decorating the PAG boundaries. These inclusions are associated with defects such as cracks in the inclusions themselves and voids at the inclusion/matrix interface. Hence, to identify the weak microstructural links, an investigation on the microstructural contribution to cleavage fracture initiation and propagation micromechanisms has been carried out on thick-section high-strength S690QL steel. Furthermore, the effect of notch orientation,

through-thickness location, and crack tip constraint on fracture toughness was analysed. The following key conclusions can be drawn from this study:

1. Large Nb-rich inclusions, some of which are distributed as clusters, act as weak microstructural links in the studied S690QL high-strength steel. For the middle section, Nb-rich inclusions are found to initiate fracture in 78% of specimens and are responsible for the worse cleavage fracture performance. For the top section, (Mg,Al,Ca)(O,S) inclusions trigger fracture in 73% of the specimens and the rest is attributed to Nb-rich inclusions. In both top and middle sections, the highest CTOD values were associated with fracture process initiated by oxide inclusions, while the lowest CTOD values were mainly found to be related to the fracture process initiated from Nb-rich inclusions. This confirms the detrimental effect of the Nb-rich particles.
2. The pre-existing cracks in the Nb-rich inclusions themselves and/or in their interface with the

matrix may serve as Griffith cracks. In this case, the crack propagation from the inclusion into the matrix is the dominant fracture step in the middle section, also contributing to lower fracture toughness.

3. Very detrimental microstructural features are observed to influence the material's fracture response to plastic constraint, also affecting the fracture micromechanisms. Contrary to the expected increase in fracture toughness with the reduction of plastic constraint (lower a/W) as observed for the top section, the CTOD values of shallow-cracked specimens extracted from the middle section remained very low. Due to the significant detrimental effect of Nb-rich inclusions, T_0 is -41 °C for the middle and -101 °C for the top. In other words, the middle section is near or at the lower shelf area of the ductile–brittle transition, while the top section is around the transition region. In this case, less plasticity is involved in fracture process of the middle section and the influence of the constraint in the fracture toughness is much lower than for the top section. Hence, in embrittled microstructures, where plasticity is limited, the low constraint at the crack tip has no considerable contribution to fracture toughness.
4. Although fracture is predominantly transgranular, 36% of specimens showed areas of intergranular fracture affecting the cleavage crack propagation. PAG boundaries in intergranularly fractured areas were found to be enriched with elements such as C, Cr, Mn, Ni, and P. However, these elements were also measured in the transgranular areas located around the intergranular ones. This may suggest that, in areas where the elemental segregation at PAG boundaries is not sufficient to embrittle the grain boundaries, the presence of Nb-rich inclusions decorating the PAG boundaries is a necessary and most likely a sufficient condition to weaken the grain boundaries, leading to intergranular fracture.
5. Fractographic profile investigation showed that the transgranular fracture for the material under study occurred in the most favourable cleavage planes {001} and {110}. It was also observed that some plastic deformation took place in the cleavage fracture process, resulting in poor indexation of points in the EBSD maps due to the considerable dislocation density. These areas could not be

properly analysed as they do not provide accurate data. The crack was observed to be significantly deflected at high-angle grain boundaries, prior austenite grain, packet, and block boundaries, mostly where the neighbouring sub-structure presents a different Bain axis.

This work provides new knowledge on the effect of microstructural and experimental factors on fracture toughness and cleavage micromechanisms in a thick-section quenched and tempered S690 high-strength steel. The results obtained in this study will contribute to modelling predictions and control of structural failure as well as provide insights on microstructural design optimisation of thick-section steels assuring structural reliability to cleavage fracture. Future work will be focused on investigating the simulated coarse grained and intercritically reheated coarse grained heat affected zones in this S690QL high-strength steel. This work is aimed at gaining fundamental understanding of the most detrimental cleavage micromechanisms in welded structures.

Acknowledgements

The authors acknowledge the support in the Micro-Tough research project (n. 16350) from the Dutch Research Council (NWO) and the consortium of partners that include Allseas Engineering, Aktien-Gesellschaft der Dillinger Hüttenwerke, Lloyd's Register, The Dutch Ministry of Defence, and TNO. We acknowledge Hans Brouwer from the Joining and Additive Manufacturing group of TU Delft for the help with the use of the Scanning Auger Microprobe (SAM) equipment.

Author contributions

VB: conceptualisation, methodology, validation, formal analysis, investigation, resources, data curation, writing–original draft, writing–review and editing, visualisation. QJ: conceptualisation, methodology, software, formal analysis, resources, writing–original draft, writing–review and editing. UT: investigation, data curation, writing–review and editing. CW: conceptualisation, validation, writing–review and editing, supervision. JS: conceptualisation, validation, writing–review and editing, supervision. VP:

conceptualisation, validation, writing–review and editing, supervision, project administration.

Data availability

The raw/processed data required to reproduce these findings cannot be shared at this time as the data also form part of an ongoing study.

Declarations

Conflict of interest The authors declare that they have no known competing financial interests or personal relationships that could have appeared to influence the work reported in this paper.

Open Access This article is licensed under a Creative Commons Attribution 4.0 International License, which permits use, sharing, adaptation, distribution and reproduction in any medium or format, as long as you give appropriate credit to the original author(s) and the source, provide a link to the Creative Commons licence, and indicate if changes were made. The images or other third party material in this article are included in the article's Creative Commons licence, unless indicated otherwise in a credit line to the material. If material is not included in the article's Creative Commons licence and your intended use is not permitted by statutory regulation or exceeds the permitted use, you will need to obtain permission directly from the copyright holder. To view a copy of this licence, visit <http://creativecommons.org/licenses/by/4.0/>.

References

- [1] Taylor J, Mehmanparast A, Kulka R et al (2020) Experimental study of the relationship between fracture initiation toughness and brittle crack arrest toughness predicted from small-scale testing. *Theor Appl Fract Mech* 110:102799. <https://doi.org/10.1016/J.TAFMEC.2020.102799>
- [2] Burdekin FM, Zhao W, Tkach Y, et al. (2004) The effects of dynamic loading on structural integrity assessments. In: Health & executive research report 208
- [3] Chen JH, Cao R (2015) *Micromechanism of cleavage fracture of metals*. Butterworth-Heinemann, Boston
- [4] J.W.Morris J (1993) *Steels: For low temperature applications*. Pergamon Press, Oxford
- [5] Liu H, Zhang H, Li J (2018) Thickness dependence of toughness in ultra-heavy low-alloyed steel plate after quenching and tempering. *Metals (Basel)* 8:1–11. <https://doi.org/10.3390/met8080628>
- [6] Popovich V, Richardson IM (2015) Fracture toughness of welded thick section high strength steels. TMS 2015 144th Annual meeting & exhibition: supplemental proceedings. Springer international publishing, Cham, pp 1031–1038
- [7] Joo MS, Suh DW, Bae JH et al (2012) Experiments to separate the effect of texture on anisotropy of pipeline steel. *Mater Sci Eng A* 556:601–606. <https://doi.org/10.1016/J.MSEA.2012.07.033>
- [8] Xu J, Fan Y (2011) Effects of temperature and crack tip constraint on cleavage fracture toughness in the weld thermal simulated X80 pipeline steels. *Adv Mater Res* 197–198:1595–1598. <https://doi.org/10.4028/www.scientific.net/AMR.197-198.1595>
- [9] Matsoukas G, Cotterell B, Mai YW (1986) Hydrostatic stress and crack opening displacement in three-point bend specimens with shallow cracks. *J Mech Phys Solids* 34:499–510. [https://doi.org/10.1016/0022-5096\(86\)90014-1](https://doi.org/10.1016/0022-5096(86)90014-1)
- [10] Sorem WA, Dodds RH, Rolfe ST (1990) An analytical comparison of short crack and deep crack CTOD fracture specimens of an A36 steel. *ASTM Spec Tech Publ*. <https://doi.org/10.1520/stp18986s>
- [11] Bertolo V, Jiang Q, Scholl S et al (2022) A comprehensive quantitative characterisation of the multiphase microstructure of a thick-section high strength steel. *J Mater Sci* 57(13):7101–7126. <https://doi.org/10.1007/s10853-022-07121-y>
- [12] Wang Q, Ye Q, Wang Z et al (2020) Thickness effect on microstructure, strength, and toughness of a quenched and tempered 178 mm thickness steel plate. *Metals (Basel)* 10:1–16. <https://doi.org/10.3390/met10050572>
- [13] Pallaspuro S, Mehtonen S, Kömi J et al (2019) Effects of local grain size and inclusions on the low-temperature toughness of low-carbon as-quenched martensite. *Mater Sci Eng A* 743:611–622. <https://doi.org/10.1016/j.msea.2018.11.105>
- [14] Moore P, Yordanova B, Lu Y, Janin YJ (2019) Influence of microstructural variation in thick section steels on the characterisation of fracture toughness using sub-size specimens. In: Proceedings of the ASME 2019 38th international conference on Ocean, Offshore and Arctic Engineering OMAE 2019
- [15] Lin T, Evans AG, Ritchie RO (1986) A statistical model of brittle fracture by transgranular cleavage. *J Mech Phys Solids* 34:477–497. [https://doi.org/10.1016/0022-5096\(86\)90013-X](https://doi.org/10.1016/0022-5096(86)90013-X)

- [16] Martín-Meizoso A, Ocaña-Arizcorreta I, Gil-Sevillano J, Fuentes-Pérez M (1994) Modelling cleavage fracture of bainitic steels. *Acta Metall Mater* 42:2057–2068. [https://doi.org/10.1016/0956-7151\(94\)90031-0](https://doi.org/10.1016/0956-7151(94)90031-0)
- [17] Chen JH, Li G, Cao R, Fang XY (2010) Micromechanism of cleavage fracture at the lower shelf transition temperatures of a C–Mn steel. *Mater Sci Eng A* 527:5044–5054. <https://doi.org/10.1016/j.msea.2010.04.063>
- [18] Kroon M, Faleskog J (2005) Micromechanics of cleavage fracture initiation in ferritic steels by carbide cracking. *J Mech Phys Solids* 53:171–196. <https://doi.org/10.1016/J.JMPS.2004.05.008>
- [19] Wallin K, Nevasmaa P, Laukkanen A, Planman T (2004) Master curve analysis of inhomogeneous ferritic steels. *Eng Fract Mech* 71:2329–2346. <https://doi.org/10.1016/J.ENGFRACMECH.2004.01.010>
- [20] Andrieu A, Pineau A, Besson J et al (2012) Bimodal Beremin-type model for brittle fracture of inhomogeneous ferritic steels: theory and applications. *Eng Fract Mech* 95:84–101. <https://doi.org/10.1016/j.engfracmech.2011.10.016>
- [21] ISO (2018) ISO 12135: Metallic materials: unified method of test for the determination of quasistatic fracture toughness. 2016
- [22] ASTM International (2020) E1820: standard test method for measurement of fracture toughness
- [23] Kyada T, Shant JR, Goyal RK, Kathayat TS (2014) Understanding the delamination and its effect on charpy impact energy in thick wall linepipe steel. *J Mater Metall Eng* 4:31–39
- [24] Ruggieri C (2010) A micromechanics approach to assess effects of constraint on cleavage fracture toughness: a weibull stress model. *J Brazilian Soc Mech Sci Eng* 32:475–488. <https://doi.org/10.1590/S1678-58782010000400010>
- [25] Francois D, Pineau A (2001) Fracture of metals part 1: cleavage fracture. In: Bouchaud E, Jeulin D, Prioul C, Roux S (eds) *Physical aspects of fracture*. Kluwer Academic, pp 15–33
- [26] Sorem WA, Dodds RH, Rolfe ST (1991) Effects of crack depth on elastic-plastic fracture toughness. *Int J Fract* 47:105–126. <https://doi.org/10.1007/BF00032572>
- [27] Smith JA, Rolfe ST (1994) The Effect of Crack Depth (a) and Crack Depth to Width Ratio (a/W) on the Fracture Toughness of A553-B Steel. *J Press Vessel Technol* 116(2):115–121. <https://doi.org/10.1115/1.2929564>
- [28] CEN (2019) NEN-EN 10025–6: Hot rolled products of structural steels-Part 6: technical delivery conditions for flat products of high yield strength structural steels in the quenched and tempered condition
- [29] Bertolo VM, Jiang Q, Walters CL, Popovich VA (2020) Effect of microstructure on cleavage fracture of thick-section quenched and tempered S690 high-strength steel. In: *Characterization of minerals, metals and materials 2020*. San Diego, pp 155–168
- [30] Dawes MG, Cho G (1992) *Shallow crack fracture mechanics toughness tests and applications: first international conference*. Elsevier Science & Technology
- [31] Rak I (2016) CTOD toughness evaluation of hyperbaric repair welds made under severe conditions. *Struct Integr Life* 16:171–178
- [32] Jiang Q, Bertolo VM, Popovich VA et al (2022) Microstructure-informed statistical modelling of cleavage fracture in high strength steels considering through-thickness inhomogeneities. *Eng Fract Mech*. <https://doi.org/10.1016/j.engfracmech.2022.108432>
- [33] Doig P, Lonsdale D, Flewitt PEJ (1982) Segregation of embrittling elements to prior austenite grain boundaries in 25Cr – 1 Mo steel. *Met Sci* 16:335–344. <https://doi.org/10.1179/030634582790427488>
- [34] Lemblé P, Pineau A, Castagne JL et al (1979) Temper embrittlement in 12% Cr martensitic steel. *Met Sci* 13:496–502. <https://doi.org/10.1179/030634579790438381>
- [35] Nasim M, Edwards BC, Wilson EA (2000) A study of grain boundary embrittlement in an Fe–8 % Mn alloy. *Mater Sci Eng A* 281:56–67. [https://doi.org/10.1016/S0921-5093\(99\)00734-0](https://doi.org/10.1016/S0921-5093(99)00734-0)
- [36] Walters CL, Voormeeren LO, Janssen M, Wallin K (2013) Validation of the acceptability of 10x20 mm specimens for fracture toughness determination of high-strength steels. In: *Proceedings of the ASME 2013 32nd international conference on Ocean, Offshore and Arctic engineering*. pp 1–9
- [37] ASTM International E1921–11a: Standard test method for determination of reference temperature, T_0 , for ferritic steels in the transition range. ASTM B Stand. Doi: <https://doi.org/10.1520/E1921-05>
- [38] Griffith AA (1920) The phenomena of rupture and flow in solids. *Philos Trans R Soc A Math Phys Eng Sci C* 582–593:163–198
- [39] Gu C, Lian J, Bao Y, Münstermann S (2019) Microstructure-based fatigue modelling with residual stresses: prediction of the microcrack initiation around inclusions. *Mater Sci Eng A* 751:133–141. <https://doi.org/10.1016/j.msea.2019.02.058>
- [40] Morris JW Jr, Kinney C, Pytlewski K, Adachi Y (2013) Microstructure and cleavage in lath martensitic steels. *Sci Technol Adv Mater* 14:1–9. <https://doi.org/10.1088/1468-6996/14/1/014208>
- [41] Wang X, Wang Z, Xie Z et al (2019) Combined effect of M/A constituent and grain boundary on the impact toughness of CGHAZ and ICCGAZ of E550 grade offshore engineering steel. *Math Biosci Eng* 16:7494–7509. <https://doi.org/10.3934/mbe.2019376>

- [42] Davies PA, Randle V (2001) Combined application of electron backscatter diffraction and stereo-photogrammetry in fractography studies. *J Microsc* 204:29–38. <https://doi.org/10.1046/j.1365-2818.2001.00922.x>
- [43] Bhadeshia HKDH (2001) Bainite in steels: transformations, microstructure and properties, 2nd ed. IOM communications
- [44] Calcagnotto M, Ponge D, Demir E, Raabe D (2010) Orientation gradients and geometrically necessary dislocations in ultrafine grained dual-phase steels studied by 2D and 3D EBSD. *Mater Sci Eng A* 527:2738–2746. <https://doi.org/10.1016/j.msea.2010.01.004>
- [45] Mohseni P, Solberg JK, Karlsen M et al (2013) Application of combined EBSD and 3D-SEM technique on crystallographic facet analysis of steel at low temperature. *J Microsc* 251:45–56. <https://doi.org/10.1111/jmi.12041>
- [46] Wang C, Wang M, Shi J et al (2008) Effect of microstructural refinement on the toughness of low carbon martensitic steel. *Scr Mater* 58:492–495. <https://doi.org/10.1016/j.scriptamat.2007.10.053>
- [47] Seah MP (1976) Segregation and the strength of grain boundaries. *Proc R Soc A* 349:535–554
- [48] Ding RG, Rong TS, Knott J (2005) Grain boundary segregation of phosphorus and molybdenum in A533B steel. *Inst Mater Miner Min* 21:1255–1260. <https://doi.org/10.1179/174328405X63953>
- [49] Archie F, Li X, Zae S (2017) Micro-damage initiation in ferrite-martensite DP microstructures: a statistical characterization of crystallographic and chemical parameters. *Mater Sci Eng A* 701:302–313. <https://doi.org/10.1016/j.msea.2017.06.094>
- [50] Menyhard M, McMahan CJ Jr, Yoshioka Y (1987) A high resolution Auger electron spectroscopy study of the intergranular fracture of a temper embrittled steel. *J Vac Sci Technol A*. <https://doi.org/10.1116/1.574626>
- [51] Papworth AJ, Williams DB (2000) Segregation to prior austenite grain boundaries in low-alloy steels. *Scr Mater* 42:1107–1112. [https://doi.org/10.1016/S1359-6462\(00\)00335-3](https://doi.org/10.1016/S1359-6462(00)00335-3)
- [52] Messmer RP, Briant CL (1982) The role of chemical bonding in grain boundary embrittlement. *Acta Metall* 30:457–467. [https://doi.org/10.1016/0001-6160\(82\)90226-7](https://doi.org/10.1016/0001-6160(82)90226-7)

Publisher's Note Springer Nature remains neutral with regard to jurisdictional claims in published maps and institutional affiliations.